Influence of Functional Monomer Glutathione on Core-shell Double Heterostructured Nanocage NiO/NiFe$_2$O$_4$@Zn$_{0.76}$Co$_{0.24}$S Performances as Electrochemical Sensor for Bromisoval Determination

Jiashuai Zhu, Lele Zhang, Kang Li[*]

School of pharmacy, Guangdong Pharmaceutical University, Guangzhou 510006, China.
[*]E-mail: 554116339@qq.com

In this work, NiO/NiFe$_2$O$_4$@Zn$_{0.76}$Co$_{0.24}$S nanocages (NCs) with core-shell type double heterostructures were synthesized using a core-shell design scheme. Among them, NiO/NiFe$_2$O$_4$ cubic cores were obtained by calcination of Ni-Fe Prussian blue analogs (PBAs), and Zn-Co-like zeolitic imidazole frameworks (ZIFs) growed in situ around these cubic cores and were sulfided to obtain NiO/NiFe$_2$O$_4$@Zn$_{0.76}$Co$_{0.24}$S NCs. The composite has a large specific surface area of 249.66 m^{2}g^{-1} due to the inherited structure of the two bimetallic organic frameworks. And there is a core-shell double heterogeneous synergy between the Zn$_{0.76}$Co$_{0.24}$S NCs and p-p heterostructured NiO/NiFe$_2$O$_4$, which makes the modified electrode exhibit superior electrochemical performance for Bromisoval (BVU). In addition, glutathione (GSH) was explored to significantly enhance the electrochemical activity of BVU by nucleophilic substitution binding of its own -SH with -Br on BVU, which greatly improved the sensitivity. Then, GSH was developed as a new functional monomer, and beta-cyclodextrin (β-CD) was selected as a secondary functional monomer, and molecularly imprinted polymer (MIP) of BVU was prepared by CV electropolymerization to achieve a specific recognition of BVU. An electrochemical sensor based on NiO/NiFe$_2$O$_4$@Zn$_{0.76}$Co$_{0.24}$S NCs and MIP was constructed to detect BVU by DPV. Under the optimal conditions, the oxidation peak current of BVU was linear over the concentration range of 0.006-3.5 μM, with the limits of detection (LOD) and quantification (LOQ) of 0.28 nm and 0.933 nm, respectively. The sensitivity reached 11.0303 μA·μM^{-1}·cm^{-2}. The method has a wider linear range and lower detection limits compared to other assays for BVU. And the sensor showed excellent reproducibility, repeatability and stability and had been applied to the determination of BVU in human serum and cosmetics with satisfactory results.

1. INTRODUCTION

Bromisoval (BVU) is a sedative and muscle relaxant commonly used in the medical field and has been widely used for decades. In recent years, BVU is even gradually appearing as an additive in cosmetic products claiming sedative, soothing, and sleep-aiding effects [1]. However, studies have found that long-term exposure to BVU can lead to addiction [2], while the elemental bromine contained in BVU can accumulate in the body and form chronic toxicity, thus causing incalculable damage to the human body [3-4]. But even so, it is still in clinical use due to its efficacy, which makes monitoring of BVU critical. So far, several methods have been reported for the detection of BVU, such as high performance liquid chromatography (HPLC) [5], gas chromatography-mass spectrometry (GC-MS) [6, 7], and liquid chromatography-mass spectrometry (LC-MS) [8, 9]. However, these methods have the disadvantages of long detection time, expensive equipment, and not easy to achieve mass use in the detection process. Electrochemical analysis methods have the advantages of high sensitivity, fast response time, ease of operation and easy miniaturization [10]. So far, there is no report on the detection of BVU by electrochemical sensor.

Molecularly imprinted polymer (MIP) is a polymer compound that has specific selectivity for a predetermined template molecule. The MIP contains cavities that are complementary to the shape and chemical functional groups of the template molecule, and has a specific arrangement of functional groups that can interact with the template molecule for specific recognition [11, 12]. In addition, MIP has the advantages of simple synthesis, low cost and high sensitivity. Therefore, the combination of MIP-based and electrochemical sensor to achieve highly sensitive detection of template molecules by specific electrical signal change scenarios is a highly promising analytical detection method for current applications [13]. In situ electropolymerization is the most promising method for the preparation of molecularly imprinted electrochemical sensor at this stage [14]. However, molecularly imprinted electrochemical sensor have certain limitations, such as insufficient conductivity of the electrodes, weak catalytic ability, and poor performance of functional monomers, which will greatly reduce the sensitivity and recognition of molecularly imprinted electrochemical sensor. Therefore, it is crucial to develop new materials with high electrocatalytic ability and high conductivity and to find excellent functional monomers.

Transition metal sulfides (TMS) have received much attention because of their superior electrical conductivity, higher electrochemical activity and high specific capacity [15, 16]. In particular, ternary TMS have a lower optical band gap and higher electrical conductivity than binary TMS and homogeneous transition metal oxides (TMOs) [17]. Zeolitic Imidazolate Frameworks (ZIFs), a subgroup of metal-organic framework materials (MOFs), consist of transition metal ions (e.g., Zn, Fe, Co, and Cu) and imidazole (MeIM)-based ligands [18, 19]. ZIF is considered as a suitable template for the construction of hollow materials due to its three-dimensional (3D) open structure [20, 21]. However, hollow TMS always suffers from structural instability while accelerating ion conduction [22]. To solve this problem , many workers have compounded hollow TMS with carbon materials. For example, Yang D et al [23] derived hollow $Zn_{0.76}Co_{0.24}S@NC$ (HZCS@NC) by hydrothermal vulcanization and high temperature calcination of ZIF-67/8 and obtained excellent specific capacity and satisfactory capacity retention. So far, there is no report on the use of ternary transition metal

oxides (TMOs) as internal heterogeneous supports to enhance the stability of ZnCo-ZIF-derived hollow $Zn_{0.76}Co_{0.24}S$ structures. In recent years, ternary TMOs have attracted much attention because of the synergistic effect between the two metals resulting in a significant improvement in electrochemical performance [24]. Among them, $NiFe_2O_4$ stands out for its higher electrical conductivity and special anti-spinel structure [25], and is a good choice as a hollow heterogeneous support material. Prussian blue analogue (PBA, $M^{II}_3[M^{III}(CN)_6]_2 \cdot H_2O$) is a regular cubic framework structure with transition metal as the coordination center and C-N as the bridging ligand [26]. The stoichiometric ratio of divalent metal ions (M^{II}) to trivalent metal ions (M^{III}) in PBA is 3:2, and heterojunctions of TMO ($M^{II}O$) and spinel-type TMO ($M^{II}M^{III}_2O_4$) may be derived after high-temperature calcination [27]. For example, Xu et al [28] obtained $NiO/NiCo_2O_4$ heterojunction derived from $Ni_3[Co(CN)_6]_2$ (Ni-Co PBA) by high-temperature calcination, which has high specific capacity, good multiplicative capability and cycling stability as a capacitor material. Kang et al [29] obtained $NiO/NiFe_2O_4$ hollow nanocage heterojunctions with excellent oxygen precipitation reaction properties by calcination of $Ni_3[Fe(CN)_6]_2$ (Ni-Fe PBA) derivatives. The unique tetrahedral morphology and p-p heterojunction structure of $NiO/NiFe_2O_4$ can provide more active centers [30]. However, $NiO/NiFe_2O_4$ is prone to agglomeration, leading to the degradation of electrocatalytic performance, and its dispersion using ZnCo-ZIF-derived hollow $Zn_{0.76}Co_{0.24}S$ would be a good strategy. Therefore, it is desirable to construct a core-shell caged heterogeneous catalytic material based on NiFe-PBA and ZnCo-ZIF derived $NiO/NiFe_2O_4$ and hollow $Zn_{0.76}Co_{0.24}S$.

Glutathione (GSH) is a tripeptide composed of glutamic acid (Glu), cysteine (Cys), and glycine (Gly), with the sulfhydryl group (-SH) on Cys as its active group [31, 32]. GSH binding is an important detoxification reaction for many exogenous substances, including drugs and environmental chemicals. It has been shown that BVU is commonly used as a model substrate for human glutathione binding and acts as a probe to assess glutathione binding activity *in vivo* [33, 34], which is attributed to the ability of GSH to bind BVU via nucleophilic substitution. Therefore, it is expected that GSH will be developed as a functional monomer for specific recognition of BVU in MIP. In addition, β-cyclodextrin (β-CD) is a cyclic oligosaccharide consisting of seven D-glucopyranose units bound by 1,4-glycosidic bonds [35]. β-CD has an "inner hydrophobic, outer hydrophilic" cage-like structure and can form hydrophobic binding sites with guest molecules for specific recognition of guest molecules, and is safe and non-toxic [36, 37]. It is often used as a functional monomer in the preparation of molecularly imprinted polymers.

In this work, $NiO/NiFe_2O_4$ nanocubes with anti-spinel type were obtained by high-temperature calcination using NiFe-PBA as the precursor. Then, the ZnCo-ZIF framework formed around $NiO/NiFe_2O_4$ by in situ growth. Finally, the core-shell double heterogeneous nanocage catalytic material $NiO/NiFe_2O_4@Zn_{0.76}Co_{0.24}S$ NCs were obtained by hydrothermal sulfidation. Among them, $NiO/NiFe_2O_4$ as the core support material greatly improves the structural stability of $Zn_{0.76}Co_{0.24}S$, and the cage-like structure of $Zn_{0.76}Co_{0.24}S$ just prevents the massive aggregation of $NiO/NiFe_2O_4$ nanoparticles. Crucially, the core-shell cage heterostructure formed by $NiO/NiFe_2O_4$ with p-p heterojunction characteristics composed of p-type semiconductors NiO and $NiFe_2O_4$ as the core and $Zn_{0.76}Co_{0.24}S$ NCs as the shell is able to provide a dual power source for secondary acceleration of the fast conduction of electrons. In addition, GSH, as a newly discovered functional monomer, can bind to

-Br on BVU by nucleophilic substitution of its own -SH, which significantly enhances the electrochemical activity of BVU and has a strong specific recognition ability for BVU. Therefore, we modified $NiO/NiFe_2O_4@Zn_{0.76}Co_{0.24}S$ NCs as an electrocatalytic material on the electrode surface, used BVU as a template molecule and GSH and β-CD as functional monomers, and prepared a molecularly imprinted membrane on the material surface by electropolymerization to obtain a new molecularly imprinted electrochemical sensor for the detection of BVU, and the experimental procedure is shown in Scheme 1. Characterization the material by scanning electron microscopy (SEM), transmission electron microscopy (TEM), X-ray diffraction (XRD), X-ray photoelectron spectroscopy (XPS) and nitrogen (N_2) adsorption-desorption. Cyclic voltammetry (CV), electrochemical impedance spectroscopy (EIS) and differential pulse voltammetry (DPV) were used to evaluate the performance of the prepared electrochemical sensor. The final test results showed that the prepared novel sensor has high sensitivity and excellent selectivity for BVU and was successfully applied to the determination of BVU in actual samples such as human serum and cosmetics (including facial masks, sunscreens, and moisturizing lotions).
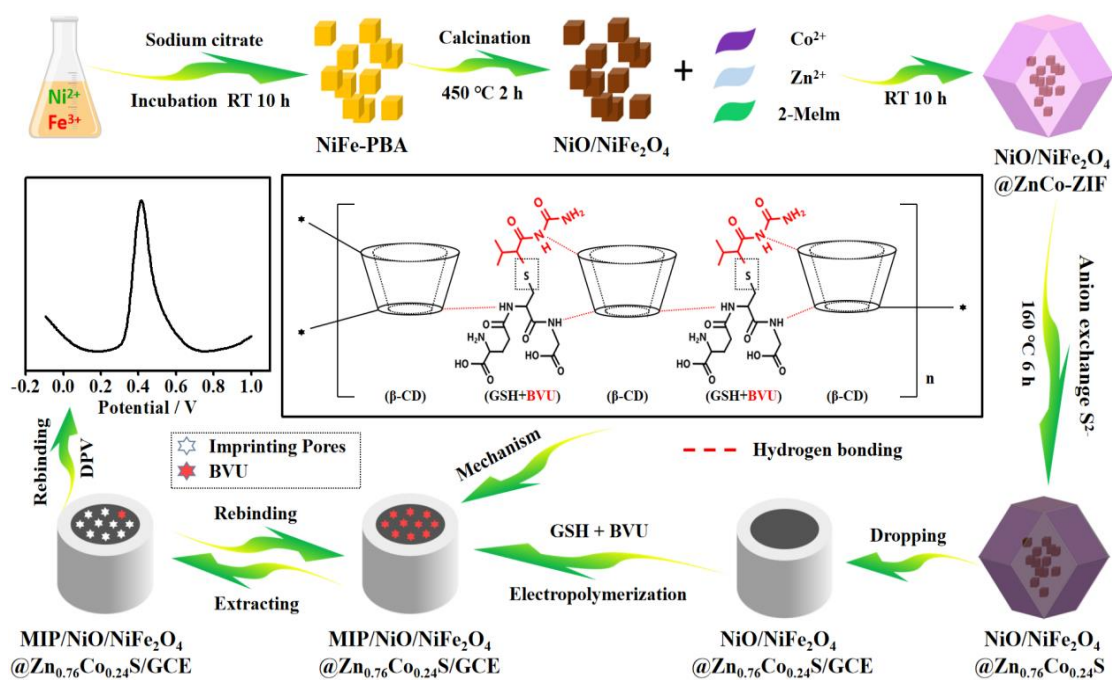
Scheme 1. Preparation of $MIP/NiO/NiFe_2O_4@Zn_{0.76}Co_{0.24}S/GCE$ and electrochemical detection process of BVU

2. EXPERIMENTAL

2.1. Reagents and apparatus

Bromisoval (BVU), reduced glutathione (GSH), β-cyclodextrin (β-CD), zinc nitrate hexahydrate and 2-methylimidazole (2-Melm) were purchased from Shanghai Maclean's Biochemical Technology (Shanghai, China). Cobalt nitrate hexahydrate, nickel chloride hexahydrate, potassium ferricyanide, sodium citrate, disodium hydrogen phosphate, sodium dihydrogen phosphate, methanol, anhydrous ethanol and isopropanol were purchased from purchased from Tianjin Zhiyuan Chemical

Reagent Co. (Tianjin, China). Thioacetamide (TAA) was purchased from Tianjin Damao Chemical Reagent Factory. Carbromal (CB), Bromhexine hydrochloride (BH), Ambroxol (AB), Ibrotamide (IBT), 4-Bromoisoquinoline (BQ) and Tiotropium bromide (TPB) were purchased from Aladdin Industries (Shanghai, China). Human serum was obtained from the First Affiliated Hospital of Guangdong Medical University. Cosmetics (including JAYJUN facial masks, UNNY CLUB sunscreens and AHC moisturizing lotions) were purchased from local cosmetic stores. All chemicals were analytically pure, and the experimental water was ultrapure water.

All electrochemical experiments in this work were done on a CHI660E electrochemical workstation (Shanghai Chenhua Instruments Co., Ltd., China). A three-electrode system was used, with a bare glassy carbon electrode (GCE) or modified GCE (3 mm diameter) as the working electrode, an Ag/AgCl/KCl electrode as the reference electrode, and a platinum (Pt) electrode as the auxiliary electrode. The PH values of the buffers were used adjusted by PHs-3C precision type PH meter (Shanghai Magnetics Instrument Factory). All weighing of the materials was done using an electronic balance type CP124C (OHAUS Instruments Ltd.). The surface morphology was characterized by scanning electron microscopy (SEM, Zeiss Supra 55) and transmission electron microscopy (TEM, JEM-2100F). X-ray photoelectron spectroscopy (XPS, EscaLab 250Xi) and X-ray diffraction (XRD, D8 ADVANCE) for elemental analysis. Brunauer-Emmett-Teller (N_2 adsorption-desorption, BET) experiments were carried out on an ASAP 2460 nitrogen adsorption specific surface area tester.

2.2. Synthesis of NiFe-PBA

The NiFe-PBA nanocubes were synthesized according to the literature [38] with slight modifications: Solution A was obtained by dissolving 0.6 mmol $NiCl_2 \cdot 6H_2O$ and 0.9 mmol sodium citrate in 20 mL ultrapure water. Solution B was obtained by dissolving 0.4 mmol of potassium ferricyanide in 20 mL of ultrapure water. Then, solution B was slowly add into solution A under stirring conditions, stirred thoroughly until homogeneous, and left to precipitate for 12 h at room temperature. After the reaction was completed, the yellow precipitate was obtained by centrifugation, washed twice with ultrapure water and anhydrous ethanol, and dried overnight in an oven at 60 ℃ to obtain NiFe-PBA.

2.3. Preparation of NiO/NiFe₂O₄ and NiO/NiFe₂O₄@ZnCo-ZIF

200 mg NiFe-PBA was calcined in air at 350 ℃ (5 ℃/min) for 2 h to obtain NiO/NiFe2O4 brown crystals.

Dissolve 3 mmol of 2-Melm in 20 mL of methanol and set aside. In addition, 10 mg of NiO/NiFe₂O₄ was ultrasonically dispersed in 20 mL of methanol, 0.75 mmol $Zn(NO_3)_2 \cdot 6H_2O$ and 0.75 mmol $Co(NO_3)_2 \cdot 6H_2O$ were added and magnetically stirred for 15 min. Then, the two solutions were mixed, stirred continuously for 3 h and then precipitate at room temperature for 20 h. The obtained precipitate was washed by centrifugation with methanol for three times and dried in an oven at 60 ℃

for 24 h to obtain $NiO/NiFe_2O_4@ZnCo$-ZIF. Under the same conditions, pure ZnCo-ZIF was obtained without the addition of $NiO/NiFe_2O_4$.

2.4. Preparation of $NiO/NiFe_2O_4@Zn_{0.76}Co_{0.24}S$ NCs

30 mg of $NiO/NiFe_2O_4@ZnCo$-ZIF and 62.7 mg of TAA were added to 35 ml of isopropanol. After stirring magnetically until homogeneous, the solution was transferred to a PTFE autoclave and reacted at 90 °C for 12 h. The obtained products were washed by centrifugation with ultrapure water and ethanol for several times, and finally placed in an oven at 60 °C for 24 h to dry, which resulted in $NiO/NiFe_2O_4@ Zn_{0.76}Co_{0.24}S$ NCs. Similarly, pure $Zn_{0.76}Co_{0.24}S$ NCs was obtained with ZnCo-ZIF.

2.5. Electrode fabrication processes

First, the bare glassy carbon electrode (GCE diameter 3 mm) was placed on a buckskin cloth and polished with alumina until it showed a glossy mirror surface, then sonicated with anhydrous ethanol and ultrapure water for 3 min, respectively. Take 1 mg of $NiO/NiFe_2O_4@Zn_{0.76}Co_{0.24}S$ in 1 mL of ultrapure water and sonicate for 15 min. 5.5 µL of $NiO/NiFe_2O_4@Zn_{0.76}Co_{0.24}S$ suspension was added dropwise to the treated GCE. Subsequently, the electrode was placed under an infrared lamp and dried to obtain $NiO/NiFe_2O_4@Zn_{0.76}Co_{0.24}S$/GCE. In the same operation, NiFe-PBA/GCE, $NiO/NiFe_2O_4$/GCE, ZnCo-ZIF/GCE, $NiO/NiFe_2O_4@ZnCo$-ZIF/GCE, and $Zn_{0.76}Co_{0.24}S$/GCE were prepared from NiFe-PBA, $NiO/NiFe_2O_4$, ZnCo-ZIF, $NiO/NiFe_2O_4@ZnCo$-ZIF, and $Zn_{0.76}Co_{0.24}S$, respectively.

The $MIP/NiO/NiFe_2O_4@Zn_{0.76}Co_{0.24}S$/GCE sensor was fabricated by immersing $NiO/NiFe_2O_4@Zn_{0.76}Co_{0.24}S$/GCE in 0.1 mol L^{-1} phosphate buffer (PBS, pH 7.0) containing 1 mM BVU, 1 mM β-CD, and 1.3 mM GSH, and scanning 12 cycles in the potential range of -0.3 to 0.8 V at a sweep rate of 65 mV S^{-1} by the CV electropolymerization method. Subsequently, the BVU-MIP electrode was immersed in a solution of methanol-acetic acid (v:v = 9:1) to remove the template molecules. Similarly, the BVU-MIP[II] electrode was fabricated without functional monomer GSH. The non-molecularly imprinted polymer modified electrode ($NIP/NiO/NiFe_2O_4@ Zn_{0.76}Co_{0.24}S$/GCE) was fabricated without template molecule BVU.

2.6. Determination of BVU in real samples

In order to be applied in practice in the future, we have selected actual samples for simulation experiments, and the experimental samples used are only simply treated as follows. 1 mL of serum was taken and diluted 50-fold with 0.1 mol L^{-1} Britton-Robinson (B-R, pH 9.2) buffer. Take 1 mL of the mask solution and dilute 100 times with 0.1 mol L^{-1} B-R (PH 9.2). Take 100 µL of moisturizing lotion and dilute 500 times with 0.1 mol L^{-1} B-R (PH 9.2) buffer. take 10 µL of sunscreen (lotion type) and dilute 1000 times with 0.1 mol L^{-1} B-R (PH 9.2) buffer. 5 mL of the above solutions were taken separately and the BVU in the samples were detected using the standard addition method.

3. RESULTS AND DISCUSSION

3.1. Materials and electrodes characterization
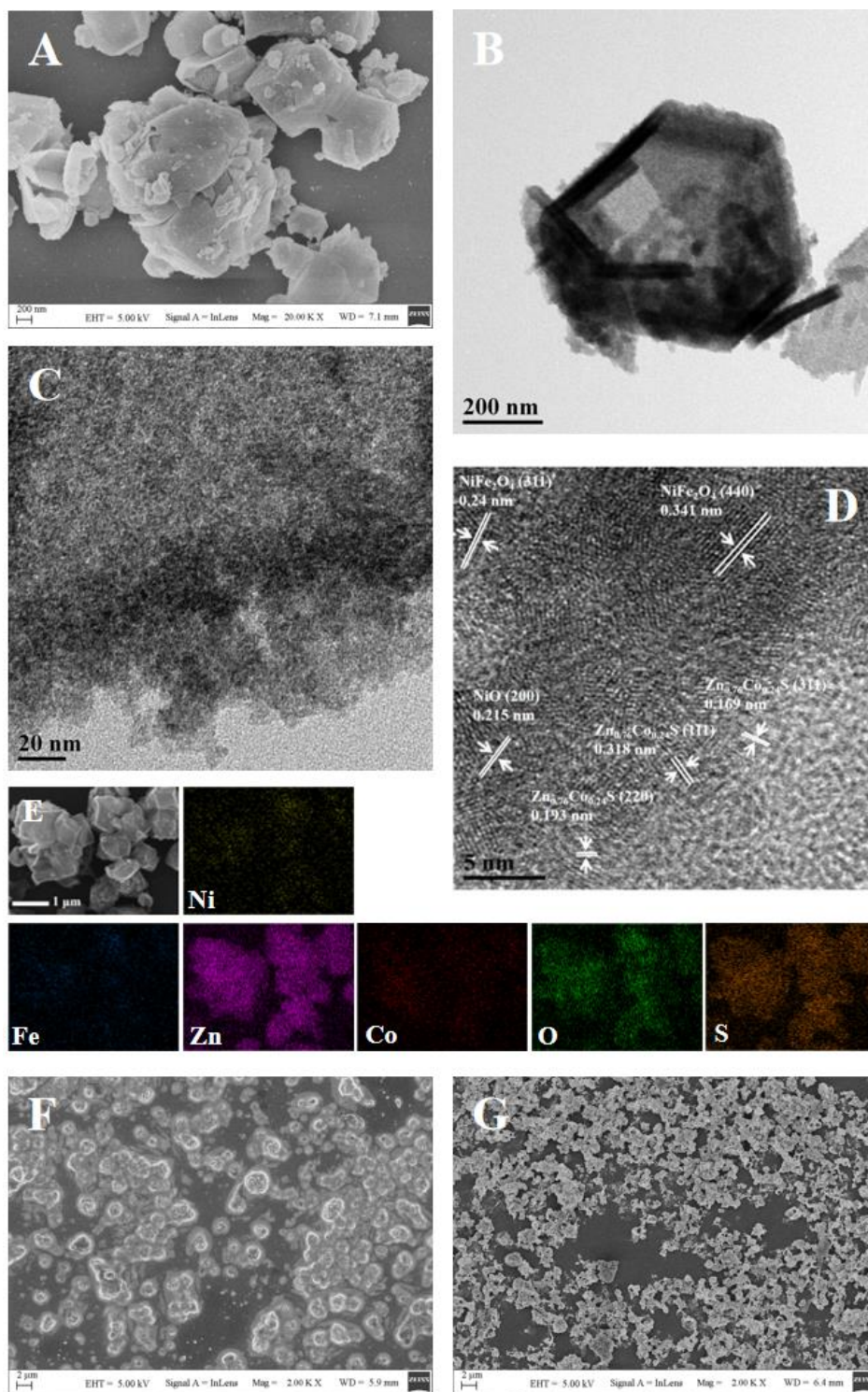
Figure 1. (A) SEM image, (B, C) TEM images, (D) HRTEM image and (E) EDX elemental mapping maps (Ni, Fe, Zn, Co, O, and S) of $NiO/NiFe_2O_4@Zn_{0.76}Co_{0.24}S$. (F) SEM images of (F) $MIP/NiO/NiFe_2O_4@Zn_{0.76}Co_{0.24}S/GCE$ before elution and (G) $MIP/NiO/NiFe_2O_4@Zn_{0.76}Co_{0.24}S/GCE$ after elution.

The surface morphology and microstructure of $NiO/NiFe_2O_4@Zn_{0.76}Co_{0.24}S$ NCs were characterized by SEM, TEM, HRTEM, and EDX. From the SEM image (Fig. 1A), it can be seen that $NiO/NiFe_2O_4@Zn_{0.76}Co_{0.24}S$ NCs is irregularly caged. Meanwhile, its surface is rougher and has tiny particles, which is attributed to the formation of $Zn_{0.76}Co_{0.24}S$ NCs after sulfidation of the ZnCo-ZIF. Further observation of the TEM images (Fig. 1B and Fig. 1C) clearly shows that the $NiO/NiFe_2O_4$ nanoparticles are uniformly arranged inside the $Zn_{0.76}Co_{0.24}S$ NCs, thus confirming what was just described. Immediately following the analysis of the HRTEM image (Fig. 1D), the stripes with lattice spacing of 0.215 nm correspond to the (200) plane of NiO[39]. The lattice stripes with spacing of 0.24 nm and 0.341 nm are attributed to the (311) and (440) planes of $NiFe_2O_4$[25, 40], respectively. The lattice spacing of 0.169 nm, 0.193 nm, and 0.318 nm lattice spacing are consistent with the (311), (220), and (111) planes of $Zn_{0.76}Co_{0.24}S$[41]. And according to the EDX mapping diagram (Fig. 1E), it shows that Ni, Fe, Zn, Co, O, and S elements are uniformly distributed throughout $NiO/NiFe_2O_4@Zn_{0.76}Co_{0.24}S$ NCs. This indicates that a core-shell double heterogeneous cage structure with $NiO/NiFe_2O_4$ with p-p heterojunction properties as the core and $Zn_{0.76}Co_{0.24}S$ NCs as the shell formed in $NiO/NiFe_2O_4@Zn_{0.76}Co_{0.24}S$ NCs.

According to the SEM image (Fig. 1F), the surface of $MIP/NiO/NiFe_2O_4@Zn_{0.76}Co_{0.24}S/GCE$ modified with BVU template molecules by CV electropolymerization presents a dense and irregular molecularly imprinted membrane, which appeared smoother overall. Interestingly, haloes of different shapes and sizes can be observed protruding from the molecularly imprinted membrane, suggesting that there are structures supported under the membrane, thus further corroborating the synthesis of $NiO/NiFe_2O_4@Zn_{0.76}Co_{0.24}S$ NCs. After the removal of BVU (Fig. 1G), the surface becomes obviously rough. The comparison between the two showed that the imprinted sites of BVU successfully formed on the $MIP/NiO/NiFe_2O_4@Zn_{0.76}Co_{0.24}S/GCE$.

The crystal structures of NiFe-PBA, $NiO/NiFe_2O_4$, $NiO/NiFe_2O_4@ZnCo$-ZIF, and $NiO/NiFe_2O_4@Zn_{0.76}Co_{0.24}S$ were investigated by XRD. As shown in Fig. 2A, all the diffraction peaks of NiFe-PBA are consistent with the previous report [42] (JCPDS no. 46-0906). The diffraction peaks of $NiO/NiFe_2O_4$, $NiO/NiFe_2O_4@ZnCo$-ZIF, and $NiO/NiFe_2O_4@Zn_{0.76}Co_{0.24}S$ are consistent with the diffraction peaks of NiO [39] (JCPDS no. 47-1049), $NiFe_2O_4$ [40] (JCPDS no. 10-0325), $Zn_{0.76}Co_{0.24}S$ (JCPDS no. 47-1656) [23], and ZnCo-ZIF [23]. The above results further demonstrate the successful synthesis of $NiO/NiFe_2O_4@Zn_{0.76}Co_{0.24}S$ composites.

The elemental composition and chemical state of $NiO/NiFe_2O_4@Zn_{0.76}Co_{0.24}S$ were studied by XPS. From Fig. 2B, it can be seen that the $NiO/NiFe_2O_4@Zn_{0.76}Co_{0.24}S$ composite is mainly composed of six elements Ni, Fe, Zn, Co, O, and S. In the Ni 2P spectrum (Fig. 2C), there are two spin-orbit double peaks (Ni $2P_{3/2}$ and Ni $2P_{1/2}$) and two satellite peaks (861.6 eV and 880.5 eV, labeled Sat.), where the binding energies 855 eV and 871.3 eV at the Ni $2P_{3/2}$ and Ni $2P_{1/2}$ peaks are attributed to Ni^{2+} and the binding energies 861.6 eV and 880.5 eV correspond to the satellite peaks of Ni $2P_{3/2}$ and Ni $2P_{1/2}$, respectively [43]. Fig. 2D shows the Fe 2P spectrum, the binding energies 711.3 eV and 718.6 eV at the characteristic peak of Fe $2P_{3/2}$, along with the binding energy 725 eV at the Fe $2P_{1/2}$ peak are attributed to Fe^{3+}. In addition, the peak at the binding energy of 718.6 eV is attributed to the satellite peak of Fe $2P_{3/2}$ [43]. Fig. 2E shows the Zn 2P profile with binding energies 1021.6 eV and 1044.7 eV attributed to Zn^{2+} at Zn $2p_{3/2}$ and Zn $2p_{1/2}$ [23].
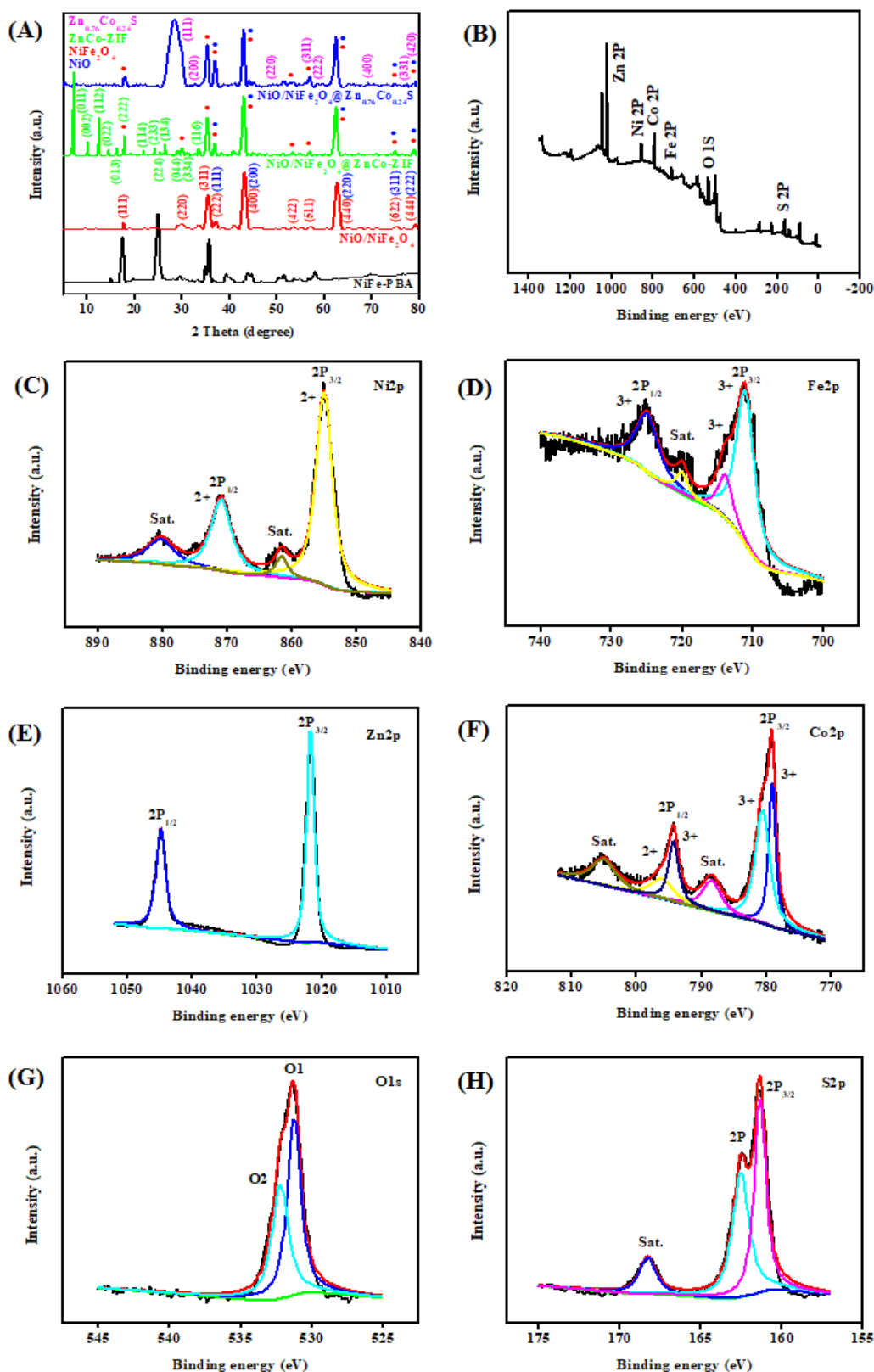
Figure 2. (A) XRD patterns of NiFe-PBA, NiO/NiFe$_2$O$_4$, NiO/NiFe$_2$O$_4$@ZnCo-ZIF and NiO/NiFe$_2$O$_4$@Zn$_{0.76}$Co$_{0.24}$S. XPS analysis of NiO/NiFe$_2$O$_4$@Zn$_{0.76}$Co$_{0.24}$S: (B) total spectrum, (C) Ni 2p, (D) Fe 2p, (E) Zn 2p, (F) Co 2p, (G) O 1s and (H) S 2p.

The Co 2P spectrum is shown in Fig. 2F, where the binding energies of 779.1 eV and 780.9 eV at the Co 2p$_{3/2}$ peak and 794.6 eV at the Co 2p$_{1/2}$ peak are attributed to Co^{3+}, while the binding energy

of 796.5 eV at the Co $2p_{1/2}$ peak is attributed to Co^{2+}, and the other two binding energies at 788.2 eV and 804.8 eV peaks were attributed to the satellite peaks of Co $2p_{3/2}$ and Co $2p_{1/2}$, respectively [41]. Two different peaks were found in the O 1s spectrum (Fig. 2G), where O1 at 531.4 eV binding energy was attributed to O^{2-}, associated with metal-oxygen bonding, and O2 at 532.1 eV binding energy was attributed to surface hydroxyl association or the presence of water molecules [40]. The S 2p spectrum is shown in Fig. 2H, where the peaks located at binding energies 161.5 eV and 162.5 eV are attributed to S $2p_{3/2}$ and S 2p, respectively, and the peak at the binding energy of 168.3 eV corresponds to the satellite peak of S 2p, thus proving the presence of S^{2-} [41].

In addition, the specific surface area and pore size distribution of the composites $NiO/NiFe_2O_4$, $Zn_{0.76}Co_{0.24}S$ and $NiO/NiFe_2O_4@Zn_{0.76}Co_{0.24}S$ were investigated by BET. Fig. 3A, B, and C show the N_2 adsorption-desorption isotherms and pore size distribution curves (inset) of $NiO/NiFe_2O_4$, $Zn_{0.76}Co_{0.24}S$, and $NiO/NiFe_2O_4@Zn_{0.76}Co_{0.24}S$ composites, respectively. The isotherms show H3-type hysteresis loops as type IV isotherms, indicating a mesoporous structure of the sample [44]. Due to the inherited skeleton structure of the two bimetallic MOFs, the surface area of $NiO/NiFe_2O_4@Zn_{0.76}Co_{0.24}S$ is 249.66 $m^2 g^{-1}$ and the average pore size is 18.71 nm, much larger than $NiO/NiFe_2O_4$ (26.11 $m^2 g^{-1}$, 10.75 nm) and $Zn_{0.76}Co_{0.24}S$ (56.91 $m^2 g^{-1}$, 7.96 nm). Meanwhile, the specific surface area of $NiO/NiFe_2O_4@Zn_{0.76}Co_{0.24}S$ is much larger than that of other common materials[23, 28, 45], thus providing a larger effective area and more active sites, thus facilitating the electrochemical reaction.
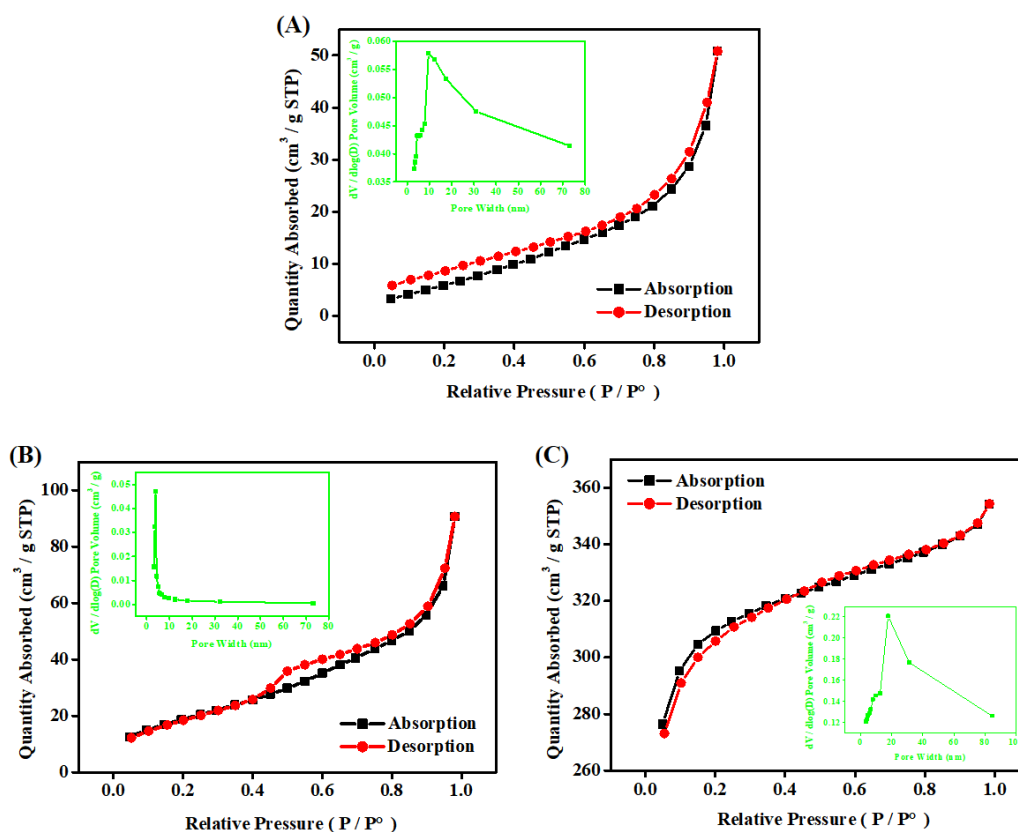
Figure 3. N_2 adsorption-desorption isotherms of (A) $NiO/NiFe_2O_4$, (B) $Zn_{0.76}Co_{0.24}S$ and (C) $NiO/NiFe_2O_4@Zn_{0.76}Co_{0.24}S$, inset shows the pore size distribution.

3.2. Electrochemical characterization of modified electrodes

Electrochemical characterization of the different modified electrodes was performed by CV and EIS in solutions containing 0.1 M KCl and 5 mM $[Fe(CN)_6]^{3-/4-}$. As shown in Fig. 4A, NiFe-PBA/GCE (b) and ZnCo-ZIF/GCE (c) exhibit weaker redox peak currents compared to the bare GCE (a), which reflects the nature of the weaker conductivity of MOF. When the precursors NiFe-PBA (calcination) and ZnCo-ZIF (sulfidation) were derived into $NiO/NiFe_2O_4$ and $Zn_{0.76}Co_{0.24}S$ composites, respectively, the peak currents of both $NiO/NiFe_2O_4$/GCE (d) and $Zn_{0.76}Co_{0.24}S$/GCE (e) were significantly enhanced and better than those of bare GCE (a), suggesting that the peak currents through MOF-derived metal oxides and sulfides have good electrical conductivity. The redox peak currents of $NiO/NiFe_2O_4@Zn_{0.76}Co_{0.24}S$/GCE (f) are significantly higher than those of bare GCE (a), $NiO/NiFe_2O_4$/GCE (d) and $Zn_{0.76}Co_{0.24}S$/GCE (e), which is attributed to the double heterogeneous structure (p-p heterogeneity, core-shell heterogeneity) possessed in $NiO/NiFe_2O_4@Zn_{0.76}Co_{0.24}S$ NCS, which greatly accelerates the electron conduction rate. When the functional monomer (GSH and β-CD) and the template molecule (BVU) are modified on the $NiO/NiFe_2O_4@Zn_{0.76}Co_{0.24}S$/GCE surface by CV electropolymerization, a dense MIP membrane formed (as in Fig. 1F), which tends to cause obstruction to the conduction of electrons. Therefore, the $MIP/NiO/NiFe_2O_4@Zn_{0.76}Co_{0.24}S$/GCE (g) shows a weak redox peak current. After removal of the template molecule (as in Fig. 1G), the peak current of $MIP/NiO/NiFe_2O_4@Zn_{0.76}Co_{0.24}S$/GCE (h) increased substantially, indicating the formation of imprinted pores of BVU on the molecularly imprinted membrane. The peak current density of $MIP^{II}/NiO/NiFe_2O_4@Zn_{0.76}Co_{0.24}S$/GCE(i) is lower than that of $NiO/NiFe_2O_4@Zn_{0.76}Co_{0.24}S$/GCE(f) when there is no functional monomer GSH. This results demonstrate that the presence of GSH can promote the transfer of electrons. In addition, the $NIP/NiO/NiFe_2O_4@Zn_{0.76}Co_{0.24}S$/GCE (j) prepared without the addition of the template molecule BVU showed a very low peak current because of the inability to form BVU-imprinted pores. The electrochemically active surface area of the modified electrode was calculated by the Randles-Sevcik equation [46, 47] as follows:

$$I_p = 2.69 \times 10^5 \, n^{3/2} \, A_{eff} \, D^{1/2} \, v^{1/2} \, C \tag{1}$$

where I_p denotes the peak oxidation current density, n is the number of electron transfers for the redox process of $[Fe(CN)_6]^{3-/4-}$ (n = 1), Aeff is the electroactive surface area (cm^2), D is the diffusion coefficient of $[Fe(CN)_6]^{3-/4-}$ ($7.6 \times 10^{-6} \, cm^2 \, s^{-1}$), v is the scan rate ($0.1 \, V \, s^{-1}$), and C is the solution $[Fe(CN)_6]^{3-/4-}$ concentration ($5 \times 10^{-6} \, mol \cdot cm^{-3}$)[48]. The electroactive surface areas of bare GCE, NiFe-PBA/GCE, ZnCo-ZIF/GCE, $NiO/NiFe_2O_4$/GCE, $Zn_{0.76}Co_{0.24}S$/GCE, $NiO/NiFe_2O_4@Zn_{0.76}Co_{0.24}S$/GCE, $MIP/NiO/NiFe_2O_4@Zn_{0.76}Co_{0.24}S$/GCE before elution, $MIP/NiO/NiFe_2O_4@Zn_{0.76}Co_{0.24}S$/GCE after elution, $MIP^{II}/NiO/NiFe_2O_4@Zn_{0.76}Co_{0.24}S$/GCE after elution, and $NIP/NiO/NiFe_2O_4@Zn_{0.76}Co_{0.24}S$/GCE were $0.0711 \, cm^2$, $0.0335 \, cm^2$, $0.0347 \, cm^2$, $0.0804 \, cm^2$, $0.0852 \, cm^2$, $0.1262 \, cm^2$, $0.0449 \, cm^2$, $0.1475 \, cm^2$, $0.1130 \, cm^2$, and $0.0411 \, cm^2$, respectively.

Fig. 4B shows the EIS results for different modified electrodes, and the inset shows the equivalent circuit diagram. where Rs represents the resistance of the solution, Rct is the charge transfer resistance, Zw is the Warburg constant, and C is the double layer capacitance. The charge transfer resistances of bare GCE, NiFe-PBA/GCE, ZnCo-ZIF/GCE, $NiO/NiFe_2O_4$/GCE, $Zn_{0.76}Co_{0.24}S$/GCE, $NiO/NiFe_2O_4@Zn_{0.76}Co_{0.24}S$/GCE, $MIP/NiO/NiFe_2O_4@Zn_{0.76}Co_{0.24}S$/GCE before elution,

MIP/NiO/NiFe$_2$O$_4$@Zn$_{0.76}$Co$_{0.24}$S/GCE after elution, MIP^{II}/NiO/NiFe$_2$O$_4$@ Zn$_{0.76}$Co$_{0.24}$S/GCE after elution, and NIP/NiO/NiFe$_2$O$_4$@Zn$_{0.76}$Co$_{0.24}$S/GCE were obtained by fitting calculations as 297.9 Ω, 1695.4 Ω, 1680.5 Ω, 206.3 Ω 178.9 Ω, 31.7 Ω, 639.8 Ω, 19.4 Ω, 87.2 Ω, and 749.8 Ω. The results are consistent with the above CV characterization results.
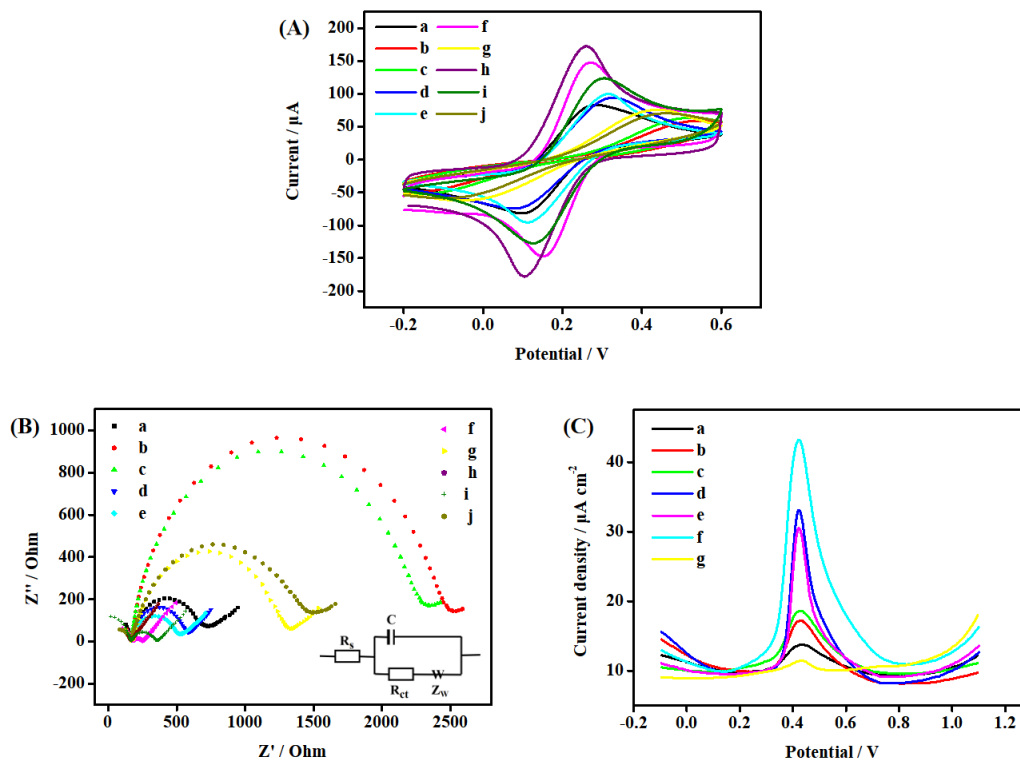
Figure 4. (A) CVs and (B) EISs recorded in 0.1 M KCl containing 5.0 mM [Fe(CN)6]$^{3-}$/$^{4-}$ for (a) bare GCE, (b) NiFe-PBA/GCE, (c) ZnCo-ZIF/GCE, (d) NiO/NiFe$_2$O$_4$/GCE, (e) Zn$_{0.76}$Co$_{0.24}$S/GCE, (f) NiO/NiFe$_2$O$_4$@Zn$_{0.76}$Co$_{0.24}$S/GCE, (g) MIP/NiO/NiFe$_2$O$_4$@Zn$_{0.76}$Co$_{0.24}$S/GCE before elution (with BVU, GSH, and β-CD), (h) MIP/NiO/NiFe$_2$O$_4$@Zn$_{0.76}$Co$_{0.24}$S/GCE after elution (with BVU, GSH, and β-CD), (i) MIP^{II}/NiO/NiFe$_2$O$_4$@Zn$_{0.76}$Co$_{0.24}$S/GCE after elution (pure BVU and β-CD) and (j) NIP/NiO/NiFe$_2$O$_4$@Zn$_{0.76}$Co$_{0.24}$S/GCE (with BVU, GSH, and β-CD). Inset: drawing of partial enlargement of EISs. The scan rate of CV was 100 mV s^{-1} and the frequency range of EIS was from 1 to 10^5 Hz with an amplitude of 5 mV. (C) DPV characterization of (a) bare GCE, (b) NiO/NiFe$_2$O$_4$/GCE, (c) Zn$_{0.76}$Co$_{0.24}$S/GCE, (d) NiO/NiFe$_2$O$_4$@Zn$_{0.76}$Co$_{0.24}$S/GCE, (e) MIP^{II}/NiO/NiFe$_2$O$_4$@Zn$_{0.76}$Co$_{0.24}$S/GCE (pure BVU and β-CD), (f) MIP/NiO/NiFe$_2$O$_4$@Zn$_{0.76}$Co$_{0.24}$S/GCE (with BVU, GSH, and β-CD), and (g) NIP/NiO/NiFe$_2$O$_4$@Zn$_{0.76}$Co$_{0.24}$S/GCE (with BVU, GSH, and β-CD) recorded in B-R buffer (pH 9.2) containing 2.7 μM BVU.

In addition, the electrochemical behavior of 2.7 μM BVU on different modified electrodes was studied using DPV in Britton-Robinson (B-R, PH 9.2) buffer. As can be seen from Fig. 4C, the oxidation peak potential of BVU on bare GCE (a) is at 0.412 V in the potential range of -0.1-1.0 V, and the peak current density is weak. When the composite materials were modified on the electrode

surfaces, the electrical signal responses of BVU on $NiO/NiFe_2O_4/GCE$ (b) and $Zn_{0.76}Co_{0.24}S/GCE$ (c) were 1.90 and 2.11 times higher than that of bare GCE (a), respectively, while the oxidation peak potential shifted left to 0.409 V. $NiO/NiFe_2O_4@Zn_{0.76}Co_{0.24}S/GCE$ (d) shows a higher BVU oxidation peak current, which is about 5.76 times higher than that of the bare GCE (a). This is attributed to the core-shell double heterogeneous cage structure and large specific surface area of $NiO/NiFe_2O_4@Zn_{0.76}Co_{0.24}S$ NCs.

The peak current density of $MIP^{II}/NiO/NiFe_2O_4@Zn_{0.76}Co_{0.24}S/GCE$ (e) was lower than that of $NiO/NiFe_2O_4@Zn_{0.76}Co_{0.24}S/GCE$ (d) when the imprinted pores of BVU formed in the MIP membrane with pure β-CD as the functional monomer. After the addition of the GSH functional monomer, $MIP/NiO/NiFe_2O_4@Zn_{0.76}Co_{0.24}S/GCE$ (f) presented the highest peak current density of about 7.85 times that of bare glassy carbon due to the ability of GSH to bind through nucleophilic substitution of its own -SH with -Br on BVU. This further demonstrates that GSH as a functional monomer can significantly enhance the electrochemical activity of BVU and promote the electron transfer. However, the $NIP/NiO/NiFe_2O_4@Zn_{0.76}Co_{0.24}S/GCE$ (g) shows a weak peak current density because the imprinted pores of BVU are not formed on the NIP membrane, which keeps the -SH on the GSH in an encapsulated closed state. In addition, the smooth NIP membrane severely hinders the electron conduction.

3.3. Optimization of $MIP/NiO/NiFe_2O_4@Zn_{0.76}Co_{0.24}S/GCE$ preparation conditions

The oxidation peak current density of the electrode in B-R (pH 9.2) buffer containing 2.7 μM BVU was used as the assessment standard, and the preparation conditions of the molecularly imprinted membrane electrode were optimized by several electrochemical experiments. The pH of PBS buffer, molar ratio of template molecule to functional monomer (BVU:β-CD:GSH), scan cycles, scan rate, elution and adsorption time were included.

First, the effect of PBS (pH 6-10) buffer on the BVU response current during the electropolymerization process was investigated. As shown in Fig. 5A, the BVU has the maximum peak current density value on the $MIP/NiO/NiFe_2O_4@Zn_{0.76}Co_{0.24}S/GCE$ at a PH value of 7.0. The number of imprinted pores in the molecularly imprinted membrane and the thickness of the membrane determine the intensity of the electrical signal response of BVU. While the ratio of template molecules to functional monomers is a key factor in determining the thickness of the molecularly imprinted membrane and the number of imprinted pores in the membrane. Therefore, we prepared several molecularly imprinted membrane electrodes according to different molar ratios of BVU to β-CD to GSH (1:1:0, 1:1:0.5, 1:1:1, 1:1:1.3, 1:1:2, 1:1:3, 1:0:1.3, 1:0.5:1.3, 1:2:1.3, and 1:3:1.3) and observed their effects on the intensity of the electrical signal response of BVU. The results are shown in Fig. 5B, where the maximum peak current density can be obtained when the molar ratio of BVU to β-CD to GSH is 1:1:1.3. This is attributed to the insufficient amount of functional monomers leading to less imprinted site formation of BVU, which in cycle leads to a weaker electrochemical response. However, excessive amounts of functional monomers lead to thicker molecularly imprinted films, which cause hindrance to the conduction of electrons. In the process of forming molecularly imprinted films by

electropolymerization, the number of scanning cycles is an important factor in determining the thickness of the molecularly imprinted film and the number of imprinted pores in the film. From Fig. 5C, it can be observed that the optimal number of scanning cycles is 12. A small number of scanning cycles will result in a thin molecularly imprinted film with only a small number of imprinted sites. Conversely, a thicker molecularly imprinted film will be obtained, which will hinder the conduction of electrons. In addition, the scanning rate is an important factor affecting the denseness of the molecularly imprinted membrane. Fig. 5D shows the highest peak current density obtained at 65 mV s^{-1}, when the imprinted pores on the MIP membrane are uniform in size and neatly ordered.
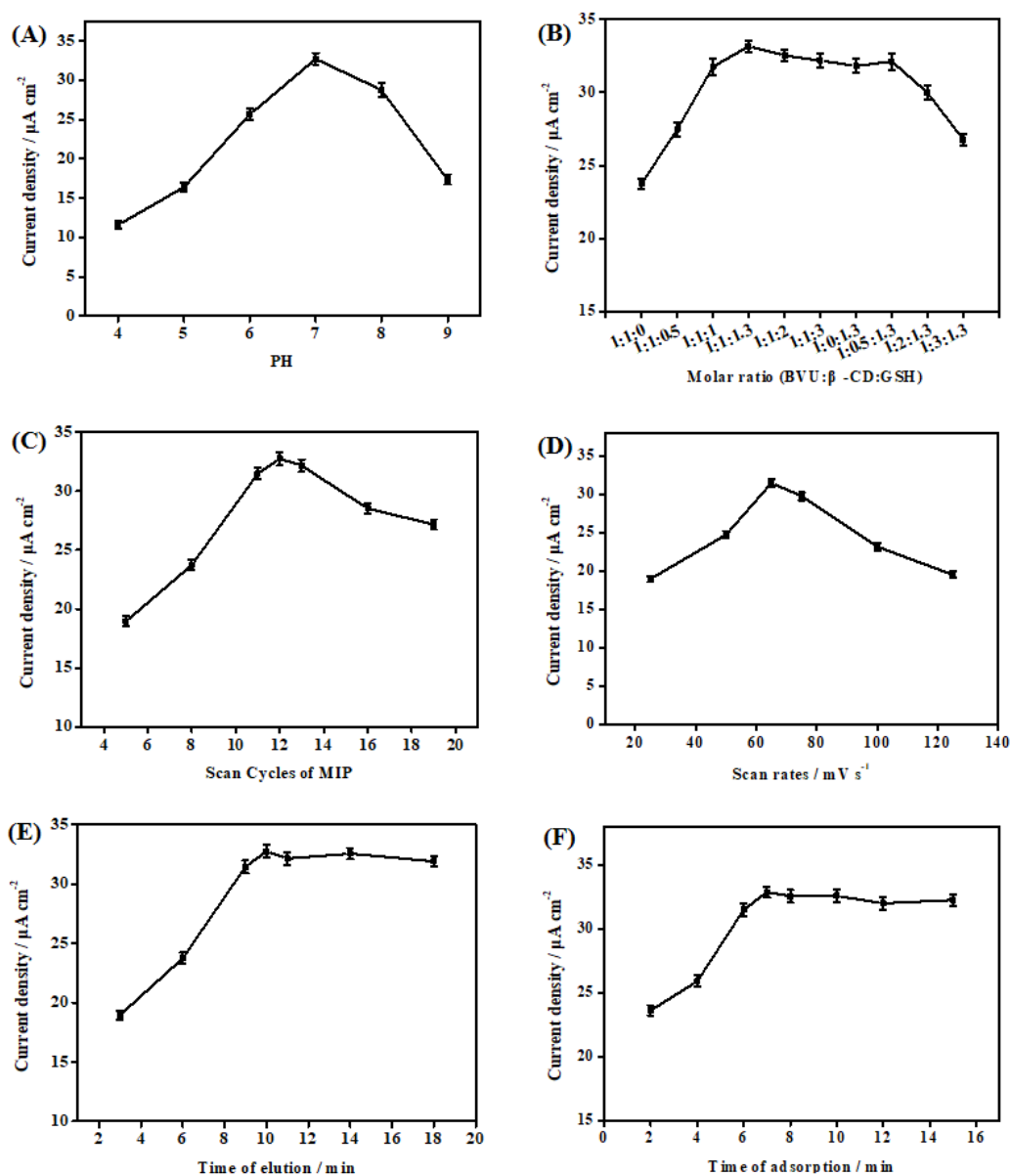
Figure 5. Effect of (A) pH of the electropolymerized PBS solution, (B) Molar ratio of BVU to β-CD to GSH, (C) scanning cycles, (D) scanning rate, (E) elution time and (F) resorption time. The above experimental conditions were explored in B-R (pH 9.2) buffer containing 2.7 μM BVU.

The elution of the template molecule BVU was completed by acetic acid-methanol (v : v = 1 : 9) solution, and then the membrane electrode with blotted pores was placed in B-R buffer (pH 9.2) containing 2.7 μM BVU for resorption. From Fig. 5E and Fig. 5F, the optimal elution time and adsorption time of the molecularly imprinted membrane were 10 min and 7 min, respectively. In BVU-MIP membrane, the imprinting sites of BVU are formed by substitution binding between -SH on BVU and -Br on BVU [33, 34], hydrogen bonding between -OH groups on β-CD and NH-groups on BVU and GSH [49], and the inclusion of hydrophobic inner lumen and hydrophilic outer lumen of β-CD [36].

3.4. Optimization of experimental conditions

3.4.1. Examination of the amount of $NiO/NiFe_2O_4@Zn_{0.76}Co_{0.24}S$ modification and the type of buffer solution

The optimal volume of $NiO/NiFe_2O_4@Zn_{0.76}Co_{0.24}S$ composite for modifying the electrode at a concentration of 1 mg/mL was first optimized. According to Fig. 6A, the response peak current density reached a maximum when the volume of the modification amount reached 5.5 μL, and the subsequent experiments were performed with this modification volume as the standard. In addition, the type of supporting electrolyte has an important influence on the redox process of the test substance at the electrode. To obtain DPV curves with high current density and low background current, different kinds of buffer solutions (pH 9.2) were examined, including Britton-Robinson (B-R) buffer, PBS buffer, Tris-HCL buffer, and sodium citrate buffer (SSC). The results are shown in Fig. 6B, which shows the best peak current density and background current in the B-R buffer.
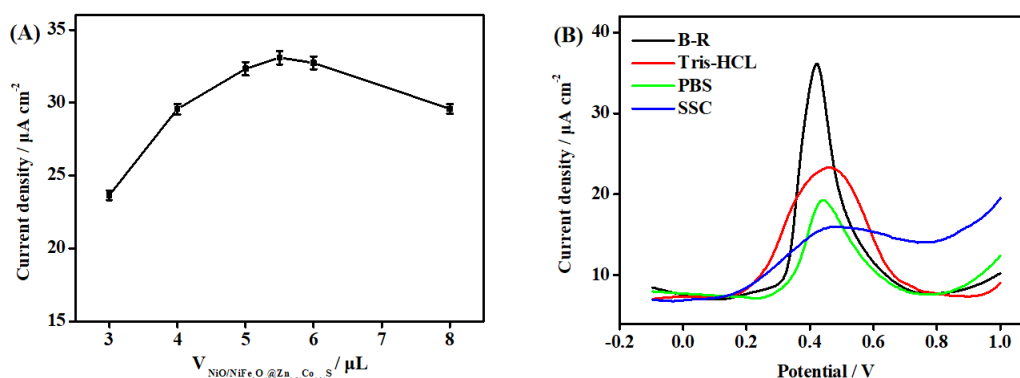
Figure 6. (A) Effect of the amount of $NiO/NiFe_2O_4@Zn_{0.76}Co_{0.24}S$ suspension modification. (B) DPV response curve of 2.3 μM BVU in B-R, Tris-HCL, PBS and SSC buffers at pH 9.2.

3.4.2. Examination of pH value of buffer solutions

The effect of B-R buffers with different pH values on the intensity of the electrical signal response of BVU was investigated by DPV. The results are shown in Fig. 7A and Fig. 7B. In the range of pH 6 to 11, the peak current density of BVU appears to increase and then decrease with the increase

of pH, and reaches the maximum value at pH 9.2. Therefore, B-R buffer (pH 9.2) was chosen for subsequent experiments. Also, it can be seen from Fig. 7A that the oxidation peak potential (E_p) of BVU continues to shift negatively with increasing pH and shows a clear linear trend (Fig. 7C). This suggests that protons are directly involved in the electrochemical oxidation of BVU, with the linear equation:

$$Ep\ (V) = 0.7942 - 0.0251PH\ (R = -0.9986) \tag{2}$$

The slope of the linear equation is 0.0251 V PH^{-1}. According to the theoretical Nernstian value (-0.059 V PH^{-1}) [50], it indicates that different numbers of electrons and protons are involved in the electrochemical oxidation reaction of BVU.
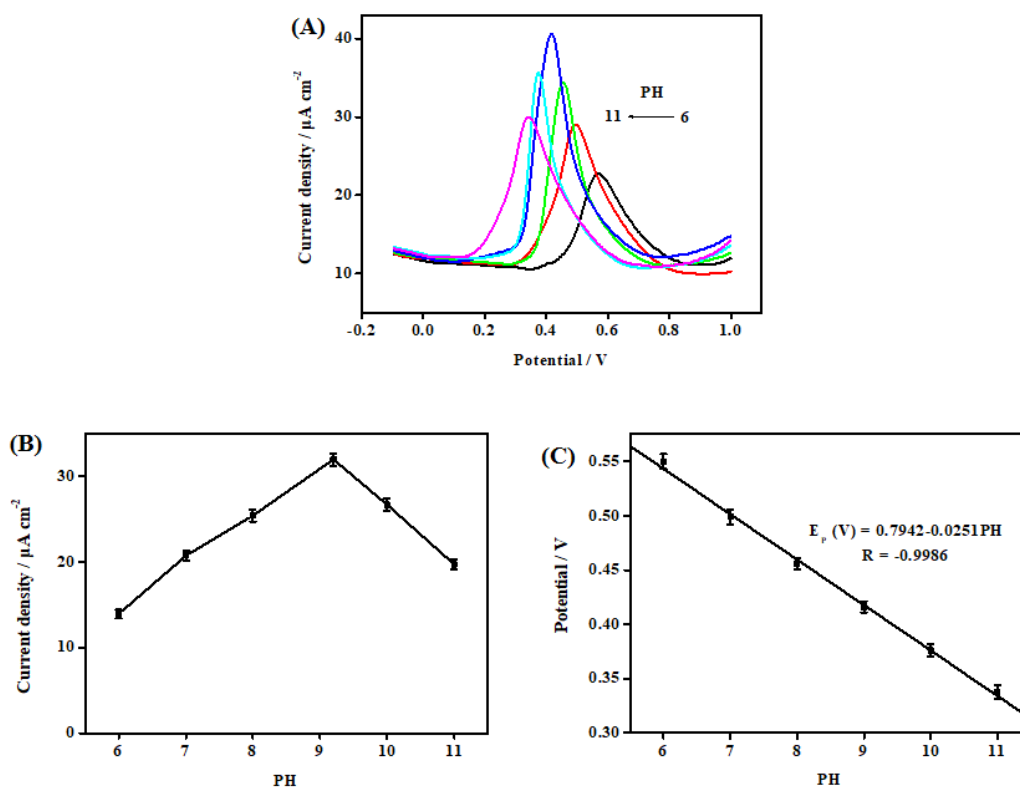
Figure 7. (A) DPV response curves of 2.7 μM BVU in B-R buffer at different pH values. pH 6.0 (black), 7.0 (red), 8.0 (green), 9.0 (blue), 10.0 (cyan), 11.0 (pink). (B) Effect of buffer pH on the oxidation peak current density of BVU. (C) Linear relationship between the oxidation peak potential Ep of BVU and buffer pH value.

3.4.3. *Examination of scanning rate*

To further explore the electron transfer process of BVU on the $MIP/NiO/NiFe_2O_4@Zn_{0.76}Co_{0.24}S/GCE$ surface, the effect of scan rate on the intensity of the electrical signal response of BVU was investigated using CV. The results are shown in Fig. 8A, where the peak oxidation current density of BVU gradually increases and the oxidation peak potential is slightly positively shifted when the scan rate is increased sequentially by 0.02 V s^{-1} in the range of 0.08-0.24 V s^{-1}. where the peak current density was linearly correlated with the scan rate (v) (Fig. 8B), indicating

that the oxidation of BVU on MIP/NiO/NiFe$_2$O$_4$@Zn$_{0.76}$Co$_{0.24}$S/GCE is an irreversible process that follows an adsorption-controlled mechanism [51]. Also, the oxidation peak potential was linearly related to the logarithm of the scan rate (lnv) (Fig. 8C), and the linear regression equation for the two was as follows:

$$J \ (\mu A \ cm^{-2}) = - 2.0445 + 130.0473v \ (V \ s^{-1}) \quad R = 0.9982 \tag{3}$$

$$E_{pa} \ (V) = 0.5189 + 0.0155 \ lnv \ (V \ s^{-1}) \quad R = 0.9983 \tag{4}$$

The number of electrons involved in the reaction can be calculated by the Laviron equation [52]:

$$E_{pa} = E_0 + \frac{RT}{\alpha nF} \ln \frac{RTk^0}{\alpha nF} + \frac{RT}{\alpha nF} \ln v \tag{5}$$

Where E_0, R, T, F, α, n, v and k^0 represent the standard electrode potential (V), gas constant (8.314 J mol^{-1} K^{-1}), temperature (298 K), Faraday constant (96500 C mol^{-1}), electron transfer coefficient, number of electrons transferred, sweep speed and electron transfer rate constant, respectively. According to the equation, the electron transfer number (n) of BVU can be calculated as 2.013 (approximately equal to 2). Combining the conclusions obtained from the linear slope of pH versus potential, it can be deduced that two electrons and one proton are involved in the oxidation reaction of BVU. The possible electrochemical oxidation mechanism of BVU at the electrode is shown in Fig. 9.
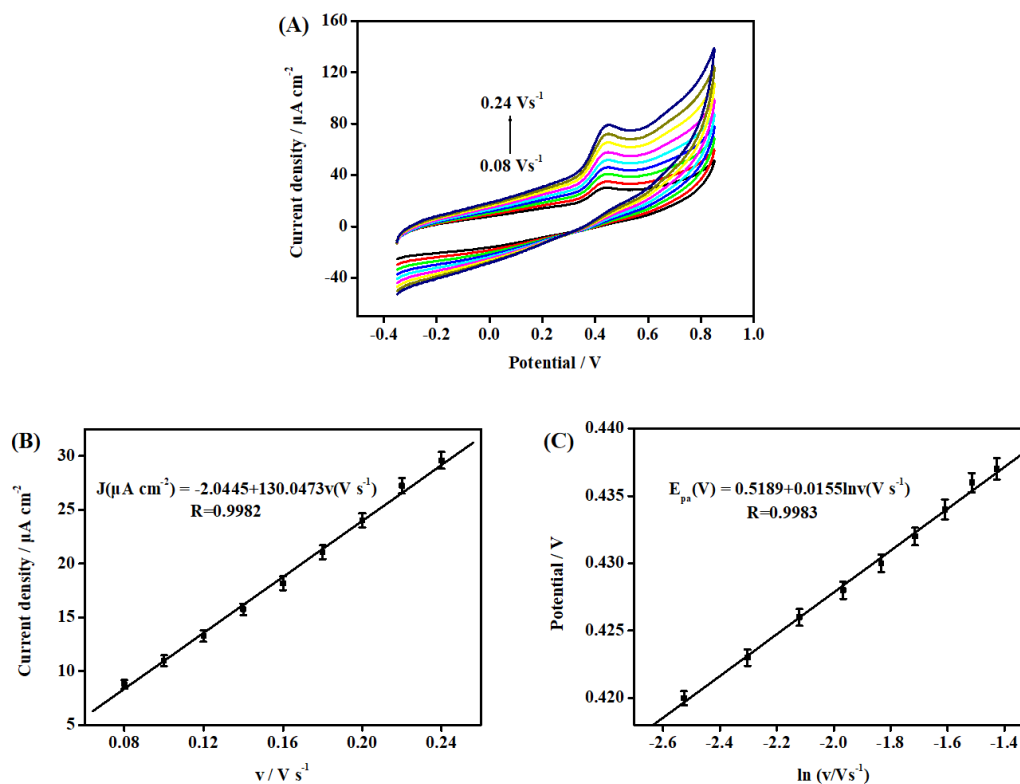
Figure 8. (A) CV response curves of 2.7 µM BVU in B-R buffer (pH 9.2) at different scan rates. scan rates: 0.08 V s^{-1}, 0.10 V s^{-1}, 0.12 V s^{-1}, 0.14 V s^{-1}, 0.16 V s^{-1}, 0.18 V s^{-1}, 0.20 V s^{-1}, 0.22 V s^{-1} and 0.24 V s^{-1}. (B) Linearity of the oxidation peak current density of BVU versus scan rate. (C) Linearity of the oxidation peak potential of BVU versus lnv.
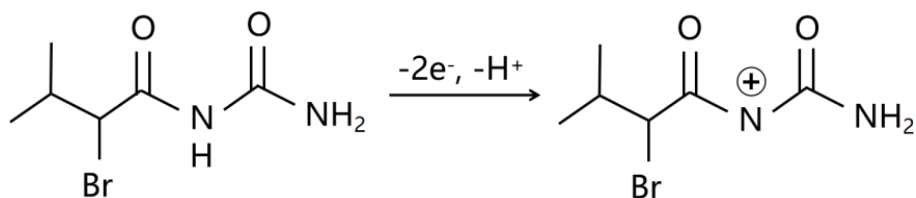
Figure 9. Schematic diagram of the electrochemical oxidation mechanism of BVU

3.4.4. Examination of the synthesis conditions of NiO/NiFe$_2$O$_4$@Zn$_{0.76}$Co$_{0.24}$S

The synthesis conditions of NiO/NiFe$_2$O$_4$@Zn$_{0.76}$Co$_{0.24}$S were optimized by DPV. The material ratio relationship of NiO/NiFe$_2$O$_4$ with zinc salt (Zn^{2+}) and cobalt salt (Co^{2+}) was firstly investigated, as shown in Fig. 10A, and the peak current density of BVU reached a maximum when the molar ratio of Zn^{2+} and Co^{2+} reached 3:3 (mmol) under the premise of quantifying NiO/NiFe$_2$O$_4$ to 40 mg. From Fig. 10B, it can be observed that the optimal mass ratio of NiO/NiFe$_2$O$_4$@ZnCo-ZIF to TAA is 1:2.1. Fig. 10C shows the optimum hydrothermal vulcanization temperature of 90 °C. What is easily noticed is that the peak current density drops sharply when the temperature exceeds 90 °C, which is attributed to the high temperature causing a large collapse of the peripheral shell layer ZnCo-ZIF during the vulcanization. Fig. 10D demonstrates the optimal hydrothermal vulcanization time of 12 h.
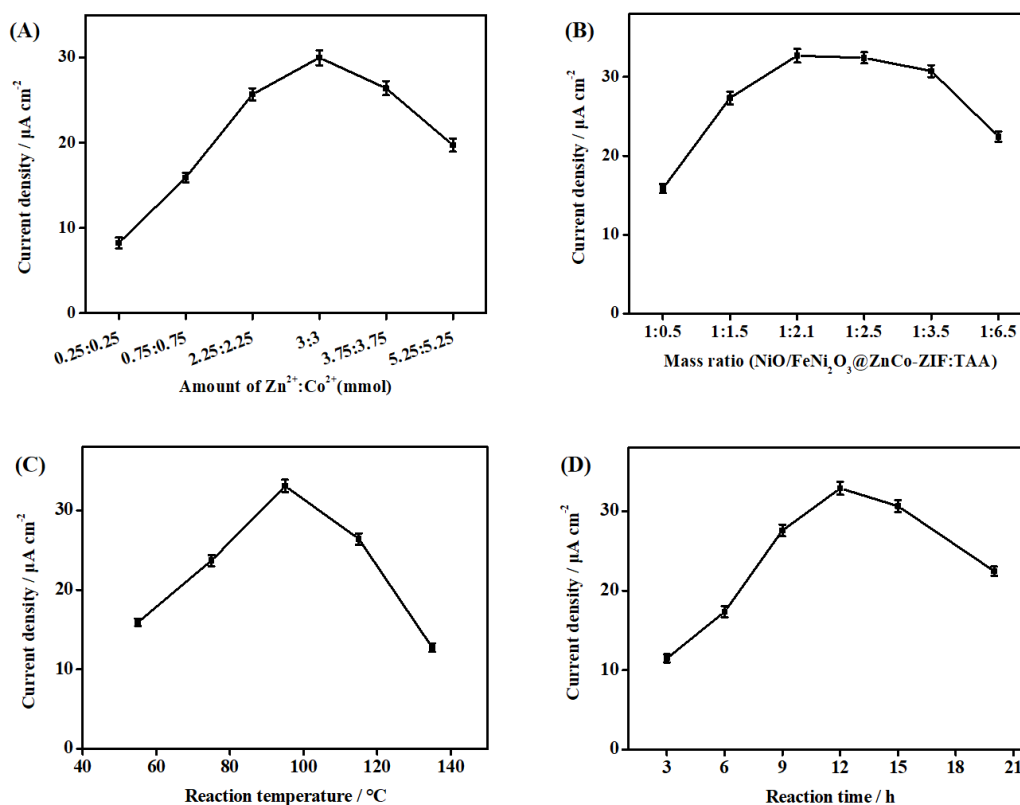
Figure 10. (A) Amount of Zn^{2+} and Co^{2+}, (B) mass ratio of NiO/NiFe$_2$O$_4$@ZnCo-ZIF to TAA, (C) vulcanization time, (D) effect of vulcanization temperature on the peak current density of BVU oxidation.

3.4.5. Linear range and detection limit of BVU

The electrochemical response of different concentrations of BVU on MIP/NiO/NiFe$_2$O$_4$@Zn$_{0.76}$Co$_{0.24}$S/GCE was studied by DPV under optimal experimental conditions. As shown in Fig. 11A, the peak current density of BVU increases linearly in the concentration range of 0.006 - 3.7 µM. The linear regression equation is shown in Fig. 11B:

$$J (\mu A\ cm^{-2}) = 3.3185 + 11.0303c\ (\mu M)\ (R = 0.9991) \tag{6}$$

Based on DL = 3σ/S (n = 10) in IUPAC, where σ denotes the standard deviation of the blank current and S denotes the slope of the linear regression equation [52, 53], the limit of quantification (LOD) was calculated to be 0.28 nm and the limit of detection (LOQ) to be 0.933 nm.

The results were compared with other reported BVU assays as shown in Table 1 [6, 8, 9]. It is obvious that our prepared MIP/NiO/NiFe$_2$O$_4$@Zn$_{0.76}$Co$_{0.24}$S/GCE sensor has higher sensitivity and wider detection range. In addition, the sensor achieves exclusive identification of BVU with fast and low cost detection.

3.4.6. Selectivity
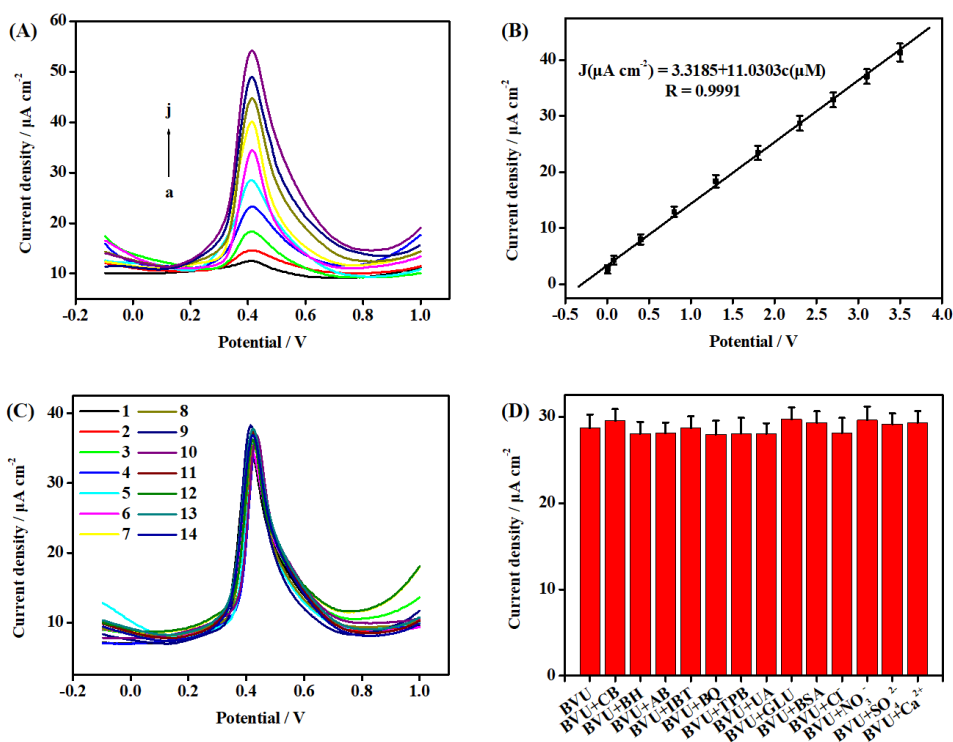
Figure 11. (A) DPV response curves recorded in 0.1 mol L-1B-R (pH 9.2) buffer for different concentrations of BVU at MIP/NiO/NiFe$_2$O$_4$@Zn$_{0.76}$Co$_{0.24}$S/GCE (1-13): 0.006, 0.08, 0.4, 0.8, 1.3, 1.8, 2.3, 2.7, 3.1, 3.5 µM. (B) Linear plot of the oxidation peak current density versus concentration for BVU. MIP/NiO/NiFe$_2$O$_4$@Zn$_{0.76}$Co$_{0.24}$S/GCE in the presence of 2.3 µM BVU or (C) DPV response curve and corresponding (D) histogram in 0.1 mol L^{-1} B-R (pH 9.2) buffer containing a certain multiple of interfering substances. 1: no interference, 2-7: 10-fold concentrations of CB, BH, AB, IBT, BQ and TPB, 8-10: 40-fold concentrations of UA, GLU and BSA, 11-14: 80-fold concentrations of Cl$^-$, NO$_3^-$, SO$_4^{2-}$ and Ca^{2+}. The error bars show the relative standard deviation of the measured values obtained from the five tests.

To verify the specific recognition ability of the MIP/NiO/NiFe$_2$O$_4$@ Zn$_{0.76}$Co$_{0.24}$S/GCE sensor for BVU, we added each of the 13 possible interferents to 0.1 mol L^{-1} B-R (pH 9.2) buffer containing 2.3 μM BVU and examined their effects on BVU peak current density by DPV repeated tests five times. Among them, six structural analogues (10-fold concentration): Carbromal (CB), Bromhexine (BH), Ambroxol (AB), Ibrotamide (IBT), 4-Bromoisoquinoline (BQ), and Tiotropium bromide (TPB). Three environmental interferents (40-fold concentration): uric acid (UA), glucose (GLU), and Bovine serum albumin (BSA). And four inorganic ions (80-fold concentration): Cl$^-$, NO$_3^-$, SO$_4^{2-}$, and Ca^{2+}. The results are satisfactory, as shown in Fig. 11C and Fig. 11D, where the peak current density of BVU fluctuates in the range of -2.55% to 3.63%, which is within the normal fluctuation range of DPV detection.

3.4.7. Reproducibility, repeatability, and stability

Similarly, the reproducibility, repeatability and stability of the MIP/NiO/NiFe$_2$O$_4$@Zn$_{0.76}$Co$_{0.24}$S/GCE sensor were examined by DPV in 0.1 mol L^{-1} B-R (pH 9.2) buffer containing 2.3 μM BVU. First, six MIP/NiO/NiFe$_2$O$_4$@Zn$_{0.76}$Co$_{0.24}$S/GCE were prepared under parallel conditions, and the six peak current density values of BVU were tested and the relative standard deviation (RSD) was calculated to be 2.83 %. Then, one electrode was randomly selected from the above six electrodes, and the BVU was tested five times repeatedly through the cyclic process of adsorption-elution-readsorption, and the RSD of the five peak current density values was calculated to be 3.57%. In addition, the MIP/NiO/NiFe$_2$O$_4$@Zn$_{0.76}$Co$_{0.24}$S/GCE was stored in a refrigerator at 4 °C for two weeks, and after testing, it was learned that the peak current density of BVU still maintained 96.15 % of its initial value. The above results show that the MIP/NiO/NiFe$_2$O$_4$@Zn$_{0.76}$Co$_{0.24}$S/GCE sensor has good reproducibility, repeatability and stability.

Table 1. Comparison of BVU detection methods

Electrode or material	Method	Linear range or LOQ	LOD	Reference
M 80-A	GC-MS	0.089-14.26 mM	0.089 mM	[6]
Symmetry C18 column	LC/MS	-	4.483 nM	[8]
DIKMA Intertsil C$_{18}$ (2.1 mm× 150 mm,5 μm)	LC-MS/MS	0.118-1.78 mM	1.2 μM	[9]
MIP/NiO/NiFe$_2$O$_4$@Zn$_{0.76}$Co$_{0.24}$S/ GCE	DPV	0.006-3.5 μM	0.28 nM	This work

3.4.8. Real sample analysis

To investigate the practicality of the $MIP/NiO/NiFe_2O_4@Zn_{0.76}Co_{0.24}S/GCE$ sensor, we applied the sensor to the determination of BVU in human serum and cosmetics (including facial masks, sunscreens and moisturizing lotions). First, three volumes of 5 ml of each solution were measured from the pre-treated actual sample standards. Using the standard addition method, 0.4 μM, 0.8 μM, and 1.8 μM of BVU were added sequentially and five parallel tests were performed. Finally, the recoveries and RSD values were calculated from the peak current density values. The results are shown in Table 2. The recoveries of BVU in serum, facial mask, sunscreen and moisturizing lotion were 99.0-102.0 %, 98.0-101.9 %, 97.5-102.4 % and 98.6-100.7 %, respectively, and the RSDs were all lower than 5 %. This indicates that the $MIP/NiO/NiFe_2O_4@Zn_{0.76}Co_{0.24}S/GCE$ sensor prepared in this work is highly accurate and reliable, and has a strong practical application value.

Table 2. Recovery of BVU in actual samples

Samples	Found (μM)	Added (μM)	Total (μM)	Recovery (%)	RSD (%)
	0	0.4	0.408	102.0	2.6
Serum	0	0.8	0.807	100.9	2.9
	0	1.8	1.782	99.0	2.1
	0	0.4	0.393	98.3	3.2
Facial mask	0	0.8	0.784	98.0	2.5
	0	1.8	1.835	101.9	3.3
	0	0.4	0.406	101.5	1.9
Sunscreen	0	0.8	0.819	102.4	2.8
	0	1.8	1.755	97.5	2.2
	0	0.4	0.395	98.6	2.8
Moisturizing lotion	0	0.8	0.799	99.9	3.5
	0	1.8	1.813	100.7	2.1

4. CONCLUSION

In this work, we first successfully synthesized $NiO/NiFe_2O_4@Zn_{0.76}Co_{0.24}S$ composites with excellent electrochemical properties by NiFe-PBA and ZnCo-ZIF. It has a large specific surface area (249.66 m2 g-1), which provides more active sites for the transfer of electrons. Moreover, the anti-spinel $NiO/NiFe_2O_4$ with p-p heterostructure is uniformly dispersed inside the $Zn_{0.76}Co_{0.24}S$ NCs, forming a core-shell double heterogeneous cage structure with a double power source, which greatly accelerates the electron conduction rate. In addition, it was explored that GSH can bind to -Br on BVU

by nucleophilic substitution of its own -SH, which significantly enhances the electrochemical activity of BVU, and at the same time has a strong and specific recognition ability for BVU. $NiO/NiFe_2O_4@Zn_{0.76}Co_{0.24}S$ NCs was used as the electrode material, BVU as the template molecule, and GSH and β-CD as the functional monomer to obtain the $MIP/NiO/NiFe_2O_4@Zn_{0.76}Co_{0.24}S/GCE$ sensor by CV electropolymerization for DPV detection of BVU. Compared with other BVU detection methods, this method obtained a wider linear range and lower detection limit. In addition, the sensor was applied to the determination of BVU in real samples with satisfactory results. This shows that the sensor has great promise for applications in the field of drug quality control and monitoring of harmful ingredients in cosmetics.

References

1. B. Dong, X. Dong, S. Liu and Y. Zhu, *Int. J. Hyg. Environ. Health.*, 6 (2016) 431.
2. C. Sun, K.A. Hollenbach and F.L. Cantrell, *Clin. Toxicol.*, 56 (2018) 653.
3. J.D. Keyser, V. Maes, R. Malfait, O. Segers and G. Ebinger, *Acta. Neurol. Belg.*, 84 (1984) 69.
4. P.C Oliveira, G.L. Adabo, F. Ricardo, S.S. Rocha, F.A. Ávila and A.L. Araújo, *Columbia. Law. Rev.*, 15 (2007) 44.
5. E. Tanaka, T. Nakamura, A. Nagashima, K. Yamazaki and S. Misawa, *J. Chromatogr. B.*, 759 (2001) 361.
6. J. Kokatsu, R. Yomoda and T. Suwa, *Chem. Pharm. Bull.*, 40 (1992) 1517.
7. A. Niederwieser, B. Steinmann and A. Matasovic, *J. Chromatogr. A.*, 147 (1978) 163.
8. H. Miyaguchi, K. Kuwayama, K. Tsujikawa, T. Kanamori and T. Kishi, *Forensic Sci. Int.*, 157 (2006) 57.
9. L.G. Jiang, K. Duo, Z.Z. Bai, Q.M. Zhang and Q.S. Zhang, *J. Pharm. Anal.*, 29 (2009) 2141.
10. M. Asif, A. Aziz, G. Ashraf, Z. Wang, J. Wang, M. Azeem, X. Chen, F. Xiao and H. Liu, *ACS Appl. Mater. Interfaces.*, 10 (2018) 36675.
11. D. Duan, H. Yang, Y. Ding, L. Li and G. Ma, *Electrochim. Acta.*, 302 (2019) 137.
12. N. Wang, S.J. Xiao and C.W. Su, *Colloid. Polym. Sci.*, 294 (2016) 1.
13. Z.A. Meng, B. Yy, A. Yw, Z.A. Bo, A. Hw, A. Gf and A. Sw, *Food Control.*, 132 (2021) 108532.
14. A. Nezhadali, L. Mehri and R. Shadmehri, *Mater. Sci. Eng. C.*, 85 (2017) 225.
15. P. Geng, S. Zheng, H. Tang, R. Zhu, L. Zhang, S. Cao, H. Xue and H. Pang, *Adv. Energy Mater.*, 8 (2018) 1703259.
16. Y. Zhao, H. Dong, X. He, J. Yu, R. Chen, Q. Liu, J. Liu, H. Zhang, R. Li and J. Wang, *J. Power Sources.*, 438 (2019) 227057.1.
17. H. Tong, W.L. Bai, S. Yue, Z. Gao, L. Lu, L. Shen, S. Dong, J. Zhu, J. He and X. Zhang, *J. Mater. Chem. A.*, 4 (2016) 11256.
18. F. Ming, H. Liang, H. Shi, X. Xu, G. Mei and Z. Wang, *J. Mater. Chem. A.*, 4 (2016) 15148.
19. X.Y. Liu and L.Z. Fan, *J. Mater. Chem. A.*, 5 (2017) 15310.
20. Y.N. Guo, J. Tang, H.Y. Qian, Z.L. Wang and Y. Yamauchi, *Chem. Mater.*, 29 (2017) 5566.
21. D. Yang, Y. Ma, C. Wang, H. Su and J. Zhang, *ChemElectroChem.*, 6 (2019) 2331.
22. Z. Chen, H. Li, R. Tian, H. Duan, Y. Guo, Y. Chen, J. Zhou, C. Zhang, R. Dugnani and H. Liu, *Sci. Rep.*, 6 (2016) 27365.

23. Y. Yang, S. Li, W. Huang, H.H. Shangguan, C. Engelbrekt, S.W. Duan, L.J. Ci and P.C. Si, *J. Mater. Chem. A.*, 7 (2019) 14670.
24. H.D. Mai, K. Rafiq and H. Yoo, *Chemistry.*, 23 (2017) 5631.
25. J. Wang, G. Yang, L. Wang and W. Yan, *J. Mater. Chem. A.*, 4 (2016) 8620.
26. T. Uemura and S. Kitagawa, *J. Am. Chem. Soc.*, 125 (2003) 7814.
27. N. Zhang, Y. Lu, Y. Fan, J. Zhou and S. Ruan, *Sens. Actuators. B.*, 315 (2020) 128118.
28. H. Xu, X. Zhao, C. Yu, Y. Sun, Z. Hui, R. Zhou, J. Xue, H. Dai, Y. Zhao and L. Wang, *Nanoscale.*, 12 (2020) 11112.
29. B.K. Kang, M.H. Woo, J. Lee, Y.H. Song, Z. Wang, Y. Guo, Y. Yamauchi, J.H. Kim, B. Lim and D.H. Yoon, *J. Mater. Chem. A.*, 5 (2017) 4320.
30. Y. Xu, X. Tian, Y. Fan and Y. Sun, *Sens. Actuators, B.*, 309 (2020) 127719.
31. G. Szalai, T. Kells, G. Galiba and G. Kocsy, *J. Plant Growth Regul.*, 28 (2009) 66.
32. N. Akter, M.A. Sobahan, M. Uraji, W. Ye and Y. Murata, *Biosci. Biotechnol Biochem.*, 76 (2012) 2032.
33. T.M.T. Mulders, V. Venizelos, R. Schoemaker, A.F. Cohen, D.D. Breimer and G.J. Mulder, *Clin. Pharmacol. Ther.*, 53 (1993) 49.
34. T.M.T. Mulders, D.J.W. Bergman, B.T. Poll-The, G.P.A. Smit and J.A.M. Smeitink, *J. Inherited Metab. Dis.*, 20 (1997) 473.
35. G.M. Duran, A.M. Contento and A. Rios, *Talanta.*, 131 (2015) 286.
36. G. Zolfaghari, *Chem. Eng. J.*, 283 (2016) 1424.
37. W.H. Tang, T.T. Ong and S.C. Ng, *J. Sep. Sci.*, 30 (2007) 1343.
38. C. Xuan, W. Jie, W. Xia, Z. Jing, Z. Peng, K. Xia, W. Xiao, H.L. Xin and D. Wang, *J. Mater. Chem. A.*, 6 (2018) 7062.
39. J.N. Liu, Q.H. Jia, J.L. Long, X.X. Wang, Z.W. Gao and Q. Gu, *Appl. Catal. B.*, 222 (2018) 35.
40. J. Zeng, T. Song, M. Lv, T.T. Wang, J.Y. Qin and H.P. Zeng, *RSC Adv.*, 6 (2016) 54964.
41. Y. Lv, A. Liu, Z. Shi, H. Che, J. Mu, Z. Guo and X. Zhang, *Chem. Eng. J.*, 349 (2018) 397.
42. Z. Gao, Y. Li, C. Zhang, S. Zhang and Y. Dong, *Anal. Chim. Acta.*, 1097 (2019) 169.
43. S. Huang, Y. Xu, T. Zhou, M. Xie, Y. Ma, Q. Liu, L. Jing, H. Xu and H. Li, *Appl. Catal. B.*, 225 (2018) 40.
44. Z. Jian, A. Zhou, S. Lun, M.C. Liu and J.R. Li, *Appl. Catal. B.*, 226 (2018) 421.
45. D. Duan, J.P. Ye and K. Li. *Sens. Actuators B.*, 344 (2021) 130222.
46. M. Asif, A. Aziz, H.T. Wang, Z.Y. Wang, W. Wei, M. Ajmal, F. Xiao, X.D. Chen and H.F. Liu, *Microchim. Acta.*, 186 (2019) 61.
47. A. Aziz, M. Asif, M. Azeem, G. Ashraf, Z.Y. Wang, F. Xiao and H.F. Liu, *Anal. Chim. Acta.*, 1047 (2019) 197.
48. M. Asif, A. Aziz, G. Ashraf, Z. Wang, J. Wang, M. Azeem, X. Chen, F. Xiao and H. Liu, *ACS Appl. Mater. Interfaces.*, 10 (2018) 36675.
49. F.F. Zhang, S.Q. Gu, Y.P. Ding, Z. Zhang and L. Li, *Anal. Chim. Acta.*, 770 (2013) 53.
50. J.W. Zhang and X. Zhang, *J. Alloys Compd.*, 842 (2020) 155934.
51. H. Chen, K. Luo and K. Li, *J. Electrochem. Soc.*, 166 (2019) B697.
52. Y. Wang, L. Yao, X. Liu, J. Cheng and H. Rao, *Biosens. Bioelectron.*, 142 (2019) 111483.
53. M. Asif, W. Haitao, D. Shuang, A. Aziz, G. Zhang, F. Xiao and H. Liu, *Sens. Actuators, B.*, 239 (2017) 243.